# Synthesis and characterization of PtCo nanowires for the electro-oxidation of methanol

Erwan Bertin, Sébastien Garbarino, Alexandre Ponrouch, Daniel Guay*

INRS – Énergie, Matériaux et Télécommunications, 1650 Boulevard Lionel-Boulet, Varennes, Québec, Canada J3X 1S2

## ABSTRACT

$Pt_xCo_{100-x}$ ($60 \leq x \leq 100$) 1D nanostructures (nanowires) on titanium are prepared by direct electrodeposition throughout a porous anodic aluminum oxide membrane and analyzed for methanol electrooxidation. For comparison, thin films of the same composition are also prepared. The morphology and composition are characterized by scanning electron microscopy (SEM) and energy dispersive X-ray spectroscopy (EDS). A model based on the simultaneous deposition of Pt and Co underpotential deposition (UPD) on Pt was devised to understand how the composition varies with the electrodeposition potential. The deposition rates were determined by means of an Electrochemical Quartz Crystal Microbalance (EQCM). $Pt_xCo_{100-x}$ alloy formation was confirmed by X-ray diffraction (XRD). Electrocatalytic properties for methanol oxidation are investigated by cyclic voltammetry (CV) in $1.0\,M\,CH_3OH + 0.5\,M\,H_2SO_4$. The results show that PtCo nanowires yield to an enhancement (by a factor of 5) of the exposed surface area ($m^2\,g^{-1}$). In the presence of $CH_3OH$, $I_f/I_b$ ratio of Pt rich nanowires is systematically higher than for thin films with the same composition. $I_f/I_b$ ratio of $Pt_{90}Co_{10}$ nanowires is 1.59, larger than that of pure Pt ($I_f/I_b = 0.76$–0.87) and commercially available PtCo deposited on carbon support ($I_f/I_b = 1.32$).

## 1. Introduction

Direct methanol fuel cell (DMFC) remains a promising portable source of energy, as the inexpensive fuel is stored in a liquid form, with a power density comparable to hydrogen/air polymer electrolyte membrane fuel cell near ambient conditions [1]. Although a lot of progress has been made in the development of DMFC, its performance is still limited by the poor kinetics and the poisoning of the anode reaction, the crossover of methanol from the anode side to the cathode side through the proton exchange membrane, the long-term stability and the cost [1–7].

Platinum is the best catalyst for the adsorption and dehydrogenation of methanol. However, poisoning of the platinum surface by reaction intermediates such as CO causes a slow deactivation of the catalyst that lowers the operating voltage. Enhanced methanol electrooxidation activity at bimetallic Pt–Ru catalysts has been extensively reported. The beneficial effect of Ru on the long-term stability of PtRu catalysts is either explained by (i) the bifunctional mechanism [8,9], where the CO-poisoned platinum is regenerated *via* a surface reaction between CO- and O-type species associated with ruthenium to yield $CO_2$, or (ii) the ligand model [8,10,11], where the presence of Ru atoms induces a change in the Pt

electronic properties, causing them to be more susceptible for OH adsorption. However, at the same loading of Pt, the power density of a DMFC using PtRu electrocatalysts at the anode is a factor of ten lower than that of a proton exchange membrane fuel cell operating on hydrogen. Alternatives must be found to find a catalyst with better performances.

In the literature, two strategies have been deployed to achieve this. The first one is based on replacing Ru by Co to form PtCo alloy catalysts. This choice is justified by the fact that, upon alloying, Co is known to modify the position of the d-band center of Pt [12], therefore affecting the strength of the Pt—CO bond and promoting the cleavage of the C—H bond at lower potential. Moreover, the presence of cobalt oxides at the surface of the catalysts provides a source of oxygen atoms that could help to mitigate the oxidation of CO at lower potential.

The second strategy is based on the use of 1D nanostructure (like nanowires) instead of 3D nanoparticles. This strategy is based on the fact that the intrinsic activity of nanoparticles varies considerably with their size. For example, it is known that the intrinsic activity (mass activity in $A\,g^{-1}_{Pt}$ and specific activity in $A\,m^{-2}_{Pt}$) of Pt nanoparticles for the oxygen reduction reaction (ORR) decreases with their diameter [13–17]. This was explained by Mayrhofer et al. [18,19], based on the fact that the energy of adsorption of oxygenated species is enhanced when the particle size is decreased. As a consequence, the increase in oxophilicity for smaller particles leads to a decrease in specific activity of the ORR, because $OH_{ad}/O_{ad}$

* Corresponding author.
  *E-mail address:* guay@emt.inrs.ca (D. Guay).

can effectively block the active sites required for the adsorption of $O_2$ and/or the splitting of the O—O bond. At the same time, the Pt utilization factor of nanoparticles increases as their size decreased and the activity (in A) of an ensemble of well dispersed nanoparticles will increase as their size is reduced. Using 1D nanostructure with typical diameter larger than 30 nm, one would hope to reduce the oxophilicity of the surface (and increase the intrinsic activity) and expose a large number of Pt atoms at the surface to get an overall high activity. The benefit of that approach was recently demonstrated using metallic 1D Pt [20,21], Ag [21] and Au [21] nanostructures that showed very interesting electrocatalytic activity for the ORR.

Similarly, it is known that the peak for adlayer CO oxidation is shifted to negative potential as the size of Pt nanoparticle is increased, that is, preadsorbed CO is easier to oxidize on larger particles than on smaller ones [18,22–24]. Again, using 1D nanostructures with typical diameter larger than *ca* 30 nm, one would hope to negatively shift the CO-stripping potential and therefore increase the tolerance of Pt to poisoning. In recent papers from our group, we showed that arrays of Pt and PtRu nanotubes and nanowires are more tolerant to CO-poisoning [25,26] than their thin films counterparts.

In this paper, we report the synthesis of arrays of bimetallic CoPt with micrometer long nanowires prepared by electrodeposition through a porous anodic aluminum oxide membrane. The composition of these 1D nanostructures can be adjusted by varying the deposition potential at a fixed composition of the deposition bath. The activity and resistance to poisoning during the electrooxidation of methanol of the bimetallic CoPt nanowires is compared with those of thin films prepared in the same conditions. Bimetallic PtCo thin films and nanowires were studied in the context of DMFC application. However, they may serve in a number of important applications ranging from novel media for magnetic information storage to electrocatalysts for hydrogen-based polymer electrolyte fuel cells.

## 2. Experimental

The deposition of Pt, Co and bimetallic Pt—Co was performed from 10 mM HCl electrolyte with 5.0 mM $Na_2PtCl_6·6H_2O$, 300 mM $CoCl_2·6H_2O$ and 5.0 mM $Na_2PtCl_6·6H_2O$ + 300 mM $CoCl_2·6H_2O$, respectively. All deposits were electroplated on Ti substrates that were prepared as described by Ponrouch et al. [27,28]. Two types of deposits were prepared: thin films (TFs) and nanowires (NWs). The films were obtained by electrodeposition on Ti substrate. The nanowires were electrodeposited through a porous AAO membrane (Anodisc 25, Whatman International Ltd.) using the experimental setup described previously [27,28]. After electrodeposition, the AAO membrane was dissolved in 1 M NaOH for 2 h at room temperature. All depositions were performed in potentiostatic mode with a Solartron SI 1287 potentiostat galvanostat. The deposition potentials are referred to the saturated calomel electrode (SCE).

The electrochemical quartz crystal microbalance (EQCM) was performed on gold-plated crystals (9 MHz AT-cut, 0.2 $cm^2$). The calibration constant determined earlier by Pb deposition was 1.15 ng $Hz^{-1}$. The plating bath used for the EQCM measurements ([$Na_2PtCl_6·6H_2O$] = 0.5 mM, [$CoCl_2·6H_2O$] = 30 mM, [HCl] = 10 mM) had lower salt concentration by a factor 10 than the plating bath used for preparation of bimetallic CoPt TFs and NWs in order to lower the deposition rates and prevent the saturation of the quartz crystal. However, the ratio between the concentration of both salts (Pt:Co) was kept constant (1:60) between the two sets of experiments.

The morphology of the deposits was studied by scanning electron microscopy (SEM) (JEOL, JSM-6300F). The composition of the deposits was assessed by energy dispersive X-ray spectroscopy (EDX). The structural characteristics of the deposit were assessed by X-ray diffraction (XRD) measurements using a Bruker D8 Advanced with Cu $K_\alpha$ radiation at 1.5418 Å.

## 3. Results and discussion

### 3.1. Morphology

Samples were prepared directly onto a titanium substrate as thin films (TFs) and through a porous AAO membrane to form an array of nanowires (NWs). The electroplating solution contains 300 mM $CoCl_2·6H_2O$ and 5.0 mM $Na_2PtCl_6·6H_2O$ in 10 mM HCl electrolyte. The effect of the deposition potential, $V_{dep}$, and of the presence of the AAO membrane on the morphology of the deposit is depicted in Fig. 1 through a series of scanning electron micrographs, where micrographs A, D and G are for depositions on a bare Ti substrate, while all the other micrographs are for depositions through the AAO membrane. The deposition potential is $V_{dep}$ = −0.2 V for micrograph A, B and C, $V_{dep}$ = −0.35 V for micrograph D, E and F, and $V_{dep}$ = −0.45 V for micrograph G, H and I. The samples deposited through the AAO membrane are shown at two different magnifications.

Electrodeposition on a bare Ti substrate yields to the formation of a thin film (Fig. 1A, D and G), while deposition through an AAO membrane yields to the formation of an array of nanowires. The morphology of the bimetallic CoPt thin film evolves from a rather smooth and compact structure for $V_{dep}$ = −0.20 V (Fig. 1A) to a deposit that presents a structure made of small interlaced particles with a high aspect ratio characteristic of a lamellar structure for $V_{dep}$ = −0.35 V (Fig. 1D). The structure of the deposit performed at $V_{dep}$ = −0.45 V (Fig. 1G) reveals some similarity with the previous one, although the deposit is denser.

Deposition through the AAO membrane yields to the formation of NWs. The fact that the deposition potential is positive or negative with respect to the reversible hydrogen potential does not seem to affect the ability to form NWs. The diameter and length of the NWs were evaluated from SEM micrographs (not shown) similar to the ones displayed in Fig. 1. In all cases, the NWs length varies from 3 to 10 μm with a diameter of 280 ± 50 nm. This value is slightly larger than that nominal value quoted by the manufacturer (200 nm) but is consistent with the diameter evaluated from SEM micrographs of the as-received membranes (not shown). It was shown elsewhere that Pt and bimetallic PtRu nanotubes could be obtained during electrodeposition though an AAO membrane giving the appropriate deposition conditions [25–28]. As far as we can tell, nanotube formation does not occur in the experimental conditions prevailing in the present study.

The composition of the various samples (thin films and nanowires) was determined by EDX and the results are shown in Fig. 2 with respect to the applied electrodeposition potential. As seen in Fig. 2, there is no difference between the composition of TF and NW prepared at any given potential. The platinum content is as low as [Pt] = 60 at% at $V_{dep}$ = −0.45 V. It increases almost linearly with the applied potential to reach [Pt] = 100 at% at $V_{dep}$ = 0.00 V. These results are consistent with those found in the literature [29]. Deposits with much lower Pt content could be prepared at still more negative deposition potentials, *e.g.* the Pt content of bimetallic CoPt prepared at −0.60, −0.80 and −1.00 V was [Pt] = 48, 30 and 5 at%, respectively. Bimetallic PtCo have been prepared by electrodeposition in that potential range [30]. However, the Co is readily dissolved and the properties of bimetallic CoPt with [Pt] < 50 at% will not be further investigated in the following sections.

As noted above, the Pt content is the same for TFs and NWs prepared in the same conditions. Since the composition of the NWs
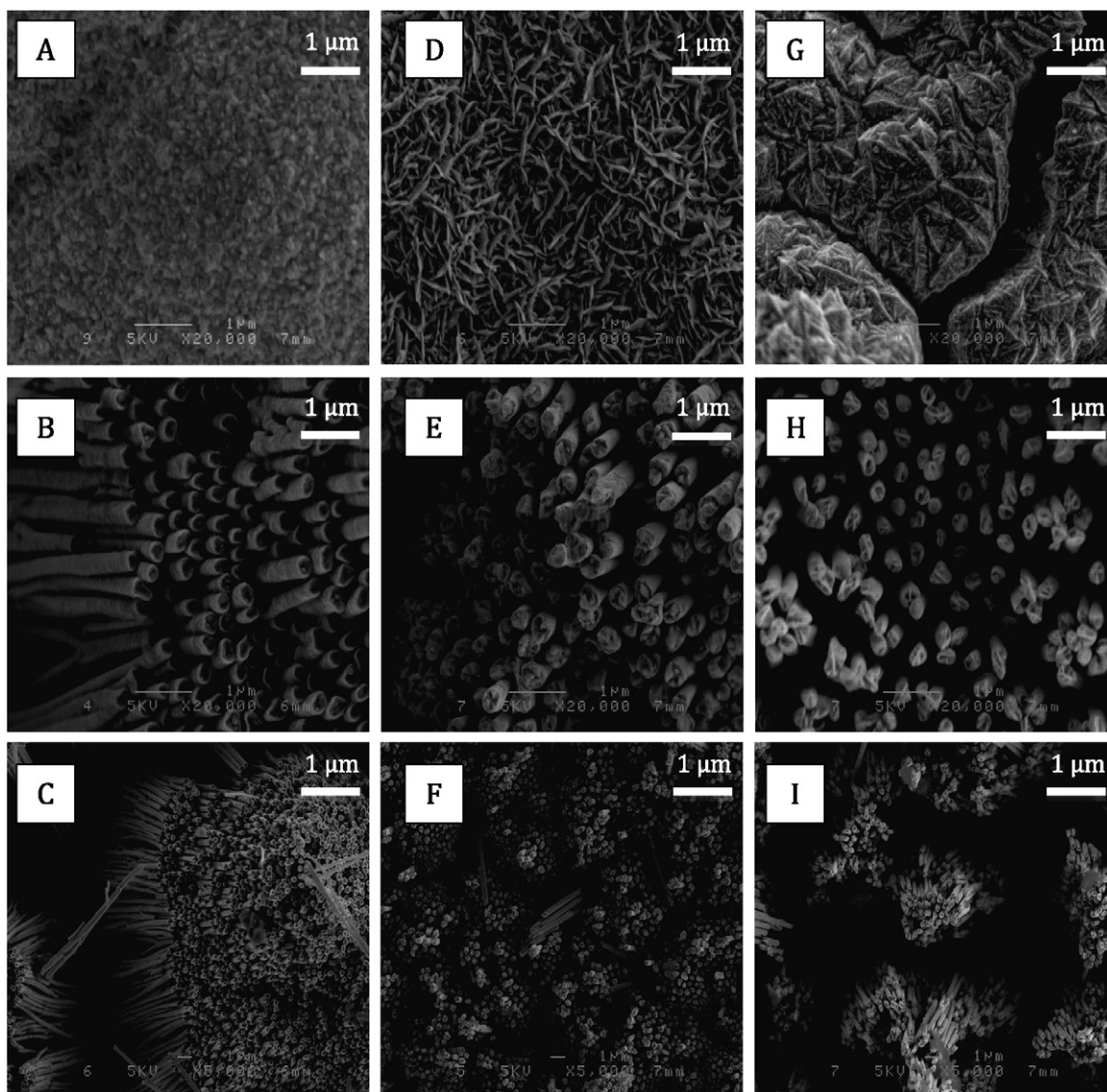
**Fig. 1.** Scanning electron microscopy micrographs of CoPt bimetallic samples deposited on a bare Ti substrate (A, D and G) and through a porous anodic aluminum oxide membrane (B, C, E, F, H and I). The deposition potential is $V_{dep} = -0.20$ V for (A, B and C), $V_{dep} = -0.35$ V for (D, E and F) and $V_{dep} = -0.45$ V for (G, H and I).

does not differ significantly from that of TFs, this indicates that diffusion of $Pt^{4+}$ and $Co^{2+}$ cations to the substrate is not hampered by the presence of the AAO membrane (or at least the diffusivity of both $Pt^{4+}$ and $Co^{2+}$ cations is affected in the same way). Therefore, the presence of the porous AAO membrane does not significantly affect the composition of the deposits but the achieved morphology is changed. The EDX results show that the composition can be controlled within a precision of ±5% by tuning the applied potential in a bath of a given composition, in agreement with previous studies [29,31].
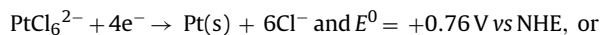
### 3.2. Deposition rate

The deposition of Pt, Co and bimetallic CoPt thin films and nanowires was further investigated by means of EQCM to determine how the deposition rates vary with the applied electrodeposition potential. In each case, 10 mM HCl electrolytes were used to determine the deposition rate of Pt (0.5 mM, $Na_2PtCl_6 \cdot 6H_2O$), Co (30 mM, $CoCl_2 \cdot 6H_2O$) and CoPt (0.5 mM, $Na_2PtCl_6 \cdot 6H_2O + 30$ mM, $CoCl_2 \cdot 6H_2O$).

Typical curves showing the mass variation measured by EQCM for Pt, Co and bimetallic CoPt deposits are presented in Fig. 3A with respect to time. The standard electrode potential ($E^0$) are given below for the two half reactions of interest

$$Co^{2+} + 2e^- \rightarrow Co(s) \text{ and } E^0 = -0.28 \text{ V } vs \text{ NHE, or}$$

$$E^0 = -0.52 \text{ V } vs \text{ SCE} \tag{1}$$

$$PtCl_6{}^{2-} + 4e^- \rightarrow Pt(s) + 6Cl^- \text{ and } E^0 = +0.76 \text{ V } vs \text{ NHE, or}$$

$$E^0 = +0.52 \text{ V } vs \text{ SCE} \tag{2}$$

The measurements were made in potentiostatic mode and the electrode potential was fixed at −0.80 V for Co and −0.10 V for both Pt and mixed Pt–Co deposits. As seen in Fig. 3A, all three curves exhibit two distinct regimes where the mass increases linearly with time. The first regime does not extend beyond *ca* 50 s and is characterized by a higher deposition rate (given by the slope of the mass *vs* time curve) than in the second regime, that extends from 50 to 300 s (the measurements were stopped after 300 s to prevent
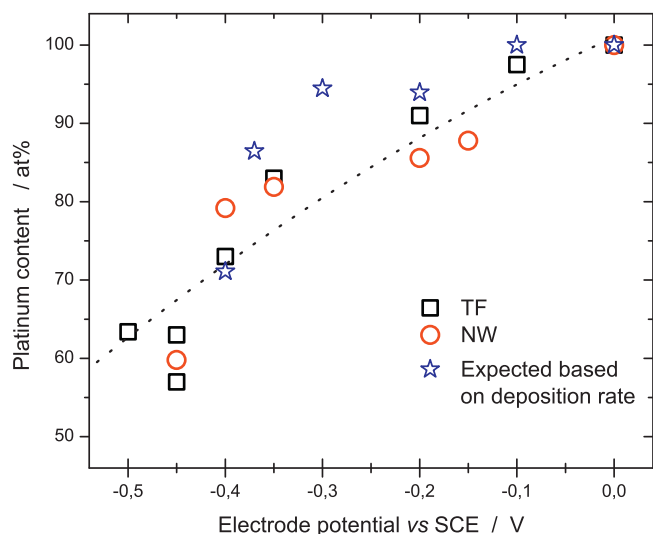
**Fig. 2.** Variation of the bulk Pt content of bimetallic CoPt samples with respect to the deposition potential. The expected composition was calculated from the deposition rates determined from EQCM measurements (details are given in the text).

saturation of the quartz crystal). The higher deposition rate at the beginning of the measurements might reflect the higher concentration of cations in the vicinity of the electrode at the beginning of the measurements. The transition between regimes 1 and 2 would then occur as steady-state deposition conditions are reached and the diffusion layer is fully established. In the following, only the deposition rate in the second (steady-state) regime will therefore be considered.
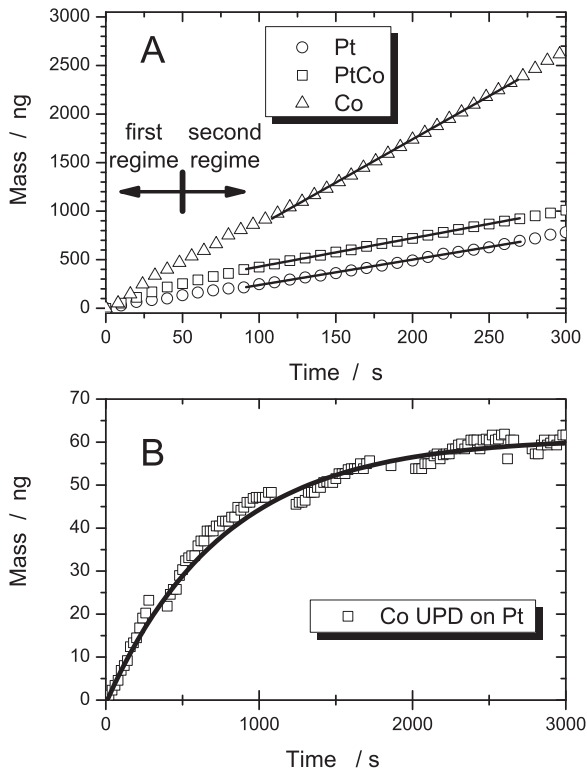


**Fig. 3.** Variation of the mass measured by EQCM with respect to time for Pt, Co and bimetallic CoPt thin films. The deposition conditions were as follows: (A) 0.5 mM Na$_2$PtCl$_6$·6H$_2$O and −0.10 V for Pt, (B) 30.0 mM CoCl$_2$·6H$_2$O and −0.80 V for Co, and (C) 0.5 mM Na$_2$PtCl$_6$·6H$_2$O + 30.0 mM CoCl$_2$·6H$_2$O and −0.10 V for bimetallic CoPt. In all cases, the supporting electrolyte was 10.0 mM HCl. The straight line indicates the region used to calculate the various deposition rates.
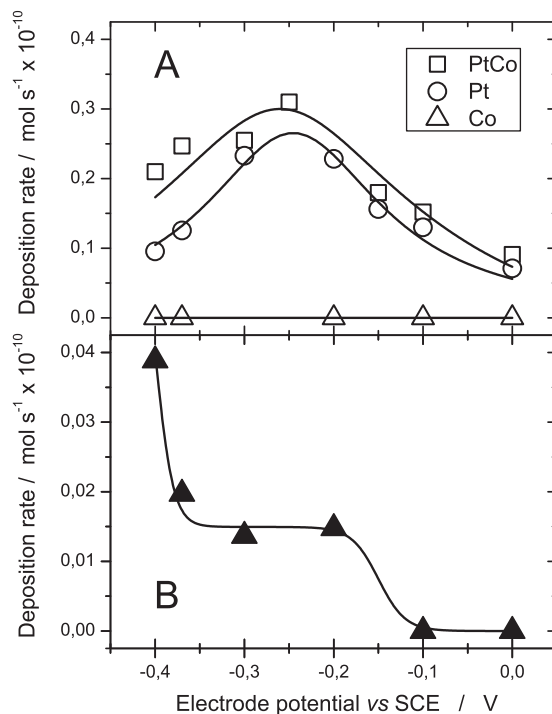


**Fig. 4.** Deposition rates as a function of the electrode potential. The deposition rates were obtained from EQCM measurements as displayed in Fig. 3.

Similar measurements were realized as a function of the deposition potential. All curves exhibited a similar behavior, independently of the electrode potential. The deposition rates of Pt, Co and Pt–Co were assessed by measuring the slope of the mass vs time curve in the second regime. The deposition rates of Pt, Co and Pt–Co films are shown in Fig. 4A.

As expected, the deposition rate of pure Co is negligible at electrode potential positive with respect to the standard electrode potential of reaction (1). The deposition of metallic Co is kinetically controlled at potential more negative than −0.52 V and an increase of the deposition rate is observed as the deposition potential is made more negative. For example, it reaches 8.7 and 113.5 × 10$^{-10}$ mole s$^{-1}$ at −0.80 and −1.00 V. However, this potential region (negative of −0.52 V) will not be investigated further.

As seen in Fig. 4A, the Pt deposition rate increases linearly from 0.00 V to −0.30 V, indicating that the deposition reaction is kinetically controlled. The Pt deposition rate is maximal at −0.30 V and decreases at more negative potential. At −0.60 V, the Pt deposition rate is low and almost identical to that recorded at −0.10 V. For large cathodic overpotential (ca $V_{dep}$ < −0.30 V) the Pt deposition rate decreases and deviates from the "ideal" behavior (constant deposition rate) expected as $V_{dep}$ reaches the potential region where the growth of the film is limited by the diffusion of Pt$^{4+}$ species to the electrode surface. This is attributed to the fact that, in our experimental conditions, hydrogen evolution starts at ca −0.30 V and may cause a chemical precipitation of Pt in the vicinity of the electrode, thereby causing a local reduction of the Pt$^{4+}$ concentration [32]. Also, for $V_{dep}$ ≤ −0.30 V, hydrogen evolution may further limit the accessibility of the electrode surface to Pt$^{4+}$ species by reducing the effective surface area between the electrode and the electrolyte. Nevertheless, in this potential range ($V_{dep}$ < −0.30 V), the growth of Pt film is limited by the diffusion of Pt$^{4+}$ species to the electrode surface.

The curve showing the variation of the deposition rate of bimetallic CoPt with respect to the electrode potential is strikingly similar to that of Pt. However, at any given potential, the

deposition rate of bimetallic CoPt is always larger than the deposition rate of pure Pt. Indeed, the difference between the two deposition rates increases slightly as the potential is made more negative. It is important to remember that the deposition rate of pure Co is zero in that potential region (see Fig. 4A). Thus the deposition rate of bimetallic CoPt is not given by the sum of the deposition rates of pure Pt and pure Co.

In principle, the composition of a bimetallic film could be calculated if the deposition rates of the two metallic species are known. Thus, assuming that there is no synergetic effect between the depositions of both metallic ions, the composition of a bimetallic CoPt deposit would be given by:

$$[Pt]_{film} = \frac{dr_{Pt}}{dr_{Pt} + dr_{Co}} \qquad (3)$$

$$[Co]_{film} = \frac{dr_{Co}}{dr_{Pt} + dr_{Co}} \qquad (4)$$

with $[Pt]_{film}$ and $[Co]_{film}$, the Pt and Co bulk content of the film, and $dr_{Pt}$ and $dr_{Co}$, the depositions rates of pure Pt and pure Co, respectively. In our case, deposition of Co, which occurs only at potentials more negative than $-0.52$ V, yields to $dr_{Co} = 0$ (see Fig. 4A) and the composition of the films and nanowires should be $[Pt]_{film} = 100\%$ for electrodeposition potentials more positive than $-0.52$ V. As shown in Fig. 2, this is not the case and the Co content of both thin films and nanowires vary systematically with the applied electrode potential from $[Co] = 40$ at% to $[Co] = 0$ at% as the applied potential is increased from $-0.50$ to $0.0$ V.

It is known that, in certain conditions, metal cations can be electrodeposited at potentials more positive than the equilibrium (Nernst) potential for the reduction of this metal. The phenomenon is called underpotential deposition (UPD). This has been observed for the deposition of Co at the surface of Pt and Au and is restricted to the deposition of less than a monolayer of Co atoms [33–37]. In order to quantify this phenomenon, the Co deposition rate on Pt in the UPD region was measured by EQCM. This was performed by first depositing a layer of Pt at the surface of a gold-coated quartz crystal microbalance. The Pt layer was prepared at $V_{dep} = -0.40$ V from 0.5 mM $Na_2PtCl_6 \cdot 6H_2O$ solution and the deposition time, $t_{dep}$, was fixed at 600 s. The hydrogen desorption charge, $Q_H$, evaluated by integration (from $-0.24$ to $0.15$ V) of the cyclic voltammogram recorded at 25 mV s$^{-1}$ in 0.5 M $H_2SO_4$ (after removing the charge corresponding to the charging of the double layer capacitance) is 0.11 mC. The roughness factor, $R_f$, of that deposit is then $R_f = 2.6$, assuming that the charge corresponding to the desorption of one monolayer of hydrogen at the surface of Pt is 0.21 mC cm$^{-2}$Pt. Then, this Pt-modified quartz crystal was contacted with a Co-containing solution (30 mM, $CoCl_2 \cdot 6H_2O$). The variation of mass as a function of time was then recorded at a series of potential that are positive with respect to the $Co^{2+}/Co$ standard electrode. In each case, a freshly prepared Pt layer was first prepared according to the details given above. A typical curve showing the variation of mass of Co underpotentially deposited on a freshly prepared Pt layer is shown in Fig. 3B for $E_{dep} = -0.20$ V.

This curve is strikingly different from that observed previously in Fig. 3A, where the mass increases linearly with time. In Fig. 3B, the instantaneous deposition rate, given by the slope of the mass vs time curve, decreases steadily and is close to nil after 2000 s. In other words, there is a finite mass of Co that can be deposited at the surface of the Pt layer. This behavior is typical of UPD of a less noble metal at the surface of a more noble metal. In the case of Fig. 3B, the total mass variation is 59.6 ng, which corresponds to 0.9 monolayer of Co at the surface of the Pt deposit (full monolayer coverage would correspond to 64.8 ng).

Similar measurements were realized in the potential range extending from 0.00 to $-0.40$ V. In each case, a freshly prepared Pt layer was prepared and contacted with a 30 mM, $CoCl_2 \cdot 6H_2O + 10$ mM HCl solution and the electrodeposition potential was varied from 0.0 to $-0.40$ V. One would have expected the mass of UPD Co to vary systematically with the potential in the UPD region but it was not possible to stress that out from our raw data. However, it must be kept in mind that each measurement was made by first depositing a freshly prepared layer of Pt at the surface of a new gold-coated quartz crystal. Accordingly, small variation of the electrochemically active surface area of this Pt layer is expected from one deposit to the other. This could translate into a non-systematic variation of the mass of Co deposited in the UPD region as the electrode potential is systematically scanned in the potential region of interest. This aspect of our work will need a more systematic study to be conducted.

Therefore, the deposition rate of Co UPD on Pt, $dr_{Co\,UPD}$, can be computed from the curve of Fig. 3B. To achieve this, the variation of mass with time was approximated by an exponential function of the form $m = A \times \exp(-t\,t^{-1}_1) + m_0$, where $A$, $t_1$ and $m_0$ are the fitted parameters. The curves corresponding to the best fit is shown as full line in Fig. 3B. As seen in that figure, the agreement between the experimental data and the fitted curve is excellent. From these curves, the deposition rate of Co at the beginning of the UPD process, can be obtained from the values of $-A\,t^{-1}_1$.

The values $dr_{Co\,UPD}$ are plotted as a function of the deposition potential in Fig. 4B. The deposition rate of Co UPD on Pt is $\sim0.02 \times 10^{-10}$ mole s$^{-1}$, a factor of 10 lower than the deposition rate of pure Pt at the same electrode potential. The fact that the values of $dr_{Co\,UPD}$ are so low compared to the deposition rate of Pt justify the linear approximation made earlier to estimate the deposition rate of Co UPD on Pt.

The expected composition of the bimetallic CoPt thin films and nanowires prepared at potential positive of the standard electrode potential of reaction (1) was then calculated from the deposition rates of Pt and Co UPD using the following equation

$$[Pt] = \frac{dr_{Pt}}{dr_{Pt} + dr_{Co\,UPD}} \times 100$$

where the Pt content is expressed in mol%. The expected Pt composition of CoPt bimetallic deposits is shown as a function of the deposition potential in Fig. 2. As seen in that figure, there is a very close correspondence between the calculated and the measured compositions, indicating the relevance of the model used to calculate them.

### 3.3. Structural characteristic

Typical XRD patterns of CoPt bimetallic thin films are shown in Fig. 5 for different values of $E_{dep}$. The diffractograms recorded on CoPt bimetallic array of nanowires (not shown) are similar. There are two series of peaks that can be attributed to either the Ti substrate or an fcc phase. No diffraction peak is observed at $2\theta = 47.34°$ that could be attributed to the main (1 0 1) diffraction peak of pure hcp Co (JCPDS card 01-089-7373) or at $2\theta = 44.23°$ that could be attributed to the main (1 1 1) diffraction peak of $\alpha$-Co (JCPDS card 01-089-4307), which is the stable form of Co at $T > 424°C$, indicating that significant amount of metallic Co is not formed during the deposition process. Therefore, it can be concluded that no significant amount of un-alloyed cobalt is present in the deposits. Instead, as seen in Fig. 5, the diffraction peaks of the fcc phase are gradually shifted to higher $2\theta$ angle value as the electrode potential is decreased (more negative). According to the results of Fig. 2, the platinum content decreases as $E_{dep}$ is more negative. Therefore, the shift observed in the position of the diffraction peaks with the electrode potential occurs as a result of a change in the composition of the fcc phase, suggesting that both Pt and Co are dissolved in this phase.
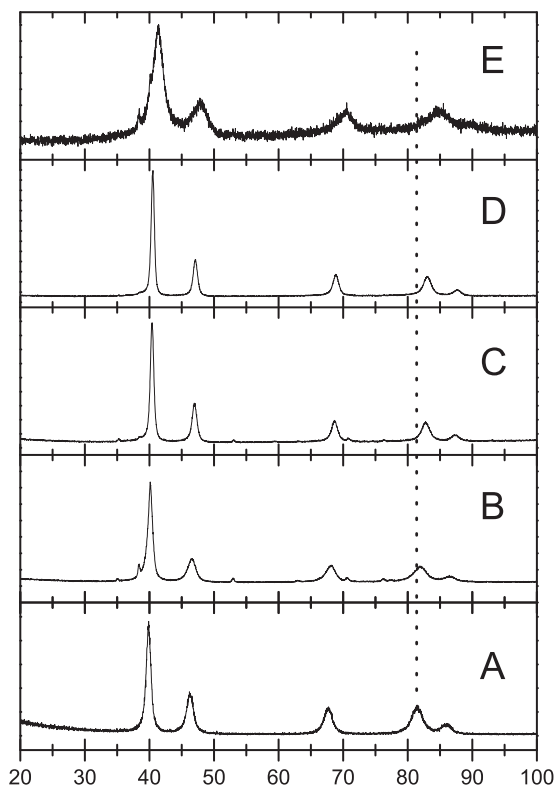
**Fig. 5.** X-ray diffraction patterns of CoPt bimetallic thin films deposited at (A) 0.0 V, (B) −0.20 V, (C) −0.35 V, (D) −0.45 V and (E) −0.60 V vs SCE.

The shift in the position of the XRD peaks is better analyzed by plotting how the lattice parameter of the fcc phase varies with the composition of the deposit. The lattice parameter of the fcc phase, $a$, was calculated from the position of the (2 0 0) diffraction peak using the Bragg Law, and Fig. 6 shows the variation of $a$ with respect to the Pt content of the deposit determined by EDX. As shown in Fig. 6, the lattice parameter $a$ decreases steadily with the Pt content. This is expected since an increase of the cobalt content will cause a proportional decrease of the lattice parameter of the fcc phase due to the smaller size of the cobalt (radius 2.506 Å) as compared to platinum (radius 2.775 Å) atoms. As seen in Fig. 6, there is a close agreement between the lattice parameter $a$ thin films and nanowires, indicating that the structure of the deposited material is not affected by
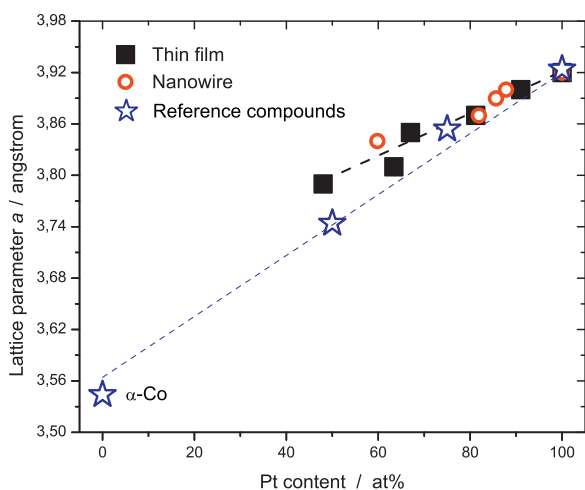


**Fig. 6.** Variation of the lattice parameter $a$ with respect to the bulk Pt content of the CoPt bimetallic deposits.

the presence of the AAO membrane that is necessary to induce the formation of nanowires.

The lattice parameter of several reference compounds is also shown in Fig. 6. Only those reference compounds having a cubic lattice have been retained. Those included: (i) α-Co, which is the stable form of pure metallic Co at $T > 424\,^\circ$C (JCPDS card 01-089-4307), (ii) fcc CoPt with a lattice parameter $a = 3.835$ Å (JCPDS card 03-065-8968), CoPt$_3$, with a lattice parameter of 3.8541 Å (JCPDS card 00-029-0499), and pure Pt with a lattice parameter of 3.9231 Å (JCPDS card 00-004-0802). As shown in Fig. 6, there is a linear relation between the lattice parameter and the composition of the bimetallic CoPt cubic reference compounds. The experimentally determined lattice parameters of the bimetallic CoPt deposits show a positive deviation with respect to that linear curve. These results are consistent with those found in the literature for Pt$_x$Co$_{100-x}$ made by different preparation methods [29,38–40].

Also, the absence of the (0 0 1) and (1 1 0) peak at $2\theta = 24^\circ$ and $2\theta = 33^\circ$, respectively, confirms that the phase formed is the high temperature fcc phase and not the $L_{10}$ low temperature phase expected from the Co—Pt binary phase diagram [38,41]. The formation of the high temperature phase for an electrodeposited alloy was already observed for CuSn and has also been reported for PtCo [40,42].

The crystallite size of both types of deposit (i.e. NWs and TFs) was evaluated from the full width at half maximum of the (2 0 0) diffraction peak of the fcc phase using the Scherrer's equation [43]. In both types of deposit, the crystallite size increases as the Pt content is reduced from 100 to 80 at%, to reach a crystallite size of ca 18 nm. Any further decrease of the Pt content results in a concomitant decrease of the crystallite size.

### 3.4. Electrochemical characterization

The cyclic voltammograms (CVs) of bimetallic CoPt in H$_2$SO$_4$ are shown in Fig. 7 for the samples prepared at different electrodeposition potentials. They were recorded at 25 mV s$^{-1}$, after a series of ca 10 cycles performed at 100 mV s$^{-1}$, during which the shape of the CVs evolved gradually to reach a steady state. All CVs exhibit the characteristic features of Pt-based compounds in H$_2$SO$_4$ electrolyte, namely (i) a hydrogen sorption region for $E < 0.10$ V and Pt oxide formation/removal for $E > 0.45$ V and (ii) a double layer charging region for $0.10 < E < 0.45$ V. The specific current (expressed in A g$^{-1}$) in the various regions remains similar for all TFs and NWs and independent of the composition, although the characteristic features of the CVs at any given composition are more salient for the bimetallic CoPt NW than for the TF. As far as we can tell, there is no systematic variation of the various electrochemical features of the CVs with the composition.

The electrochemically active surface area (EASA), expressed in terms of cm$^2$$_{Pt}$, was determined from the hydrogen adsorption/desorption charge, using a reference value of 210 μC cm$^{-2}$$_{Pt}$ for the charge corresponding to the desorption of one monolayer of H at the surface of 1 cm$^2$ of Pt. Also, in each case, the mass of the deposit was determined and the specific area, expressed in terms of m$^2$ g$^{-1}$, was calculated. These values are listed in Table 1. The specific areas of the thin films are very close to each other and independent of the composition of the bimetallic CoPt. The same assertion holds true in the case of the nanowires, although the specific area of Pt$_{80}$Co$_{20}$ is almost twice as large as the values of Pt$_{90}$Co$_{10}$ and Pt$_{60}$Co$_{40}$ NWs. As discussed previously, Pt$_{80}$Co$_{20}$ is formed by electrodeposition at $E_{dep} = -0.35$ V. At that potential, it was shown elsewhere that the structure of the deposit evolves from nanowires (less negative deposition potential) to nanotubes (more negative deposition potential) when co-deposition of Pt$^{4+}$ and Ru$^{3+}$ is performed through an AAO membrane [27,28]. Opening of a nanowire to form a nanotube has the effect of increasing

**Table 1**
Physico-chemical characteristics of PtCo thin films and nanowires.

| Deposition potential (V) | Type of deposit | [Pt]$_{Bulk}$ (at%) | Specific area (m$^2$ g$^{-1}$) | $I_f/I_b$ |
|---|---|---|---|---|
| −0.20 | TF | 90 | 3.4 ± 0.1 | 1.36 |
| −0.20 | NW | 90 | 14.7 ± 0.4 | 1.59 |
| −0.35 | TF | 80 | 3.0 ± 0.2 | 0.91 |
| −0.35 | NW | 80 | 24.4 ± 3.5 | 1.02 |
| −0.45 | TF | 60 | 2.51 ± 0.1 | 1.01 |
| −0.45 | NW | 60 | 14.7 ± 0.1 | 0.79 |

(double) the electrochemically accessible surface as the interior of the 1D nanostructure becomes accessible to the electrolyte. However, a close inspection of the SEM micrographs of Fig. 1 does not show any evidence of nanotube formation.

It was also shown elsewhere that preferentially oriented (1 0 0) Pt nanowires are formed during potentiostatic deposition of Pt$^{4+}$ cation (at −0.35 V vs SCE) through a porous AAO membrane [44]. Evidence of a preferential orientation of Pt were found in the CV of the deposit that displays a $h_2/h_1$ ratio value larger than 1, where $h_1$ and $h_2$ are the peak current for the oxidation of the weakly and strongly bonded hydrogen species at 0.13 and 0.27 V vs NHE, respectively. The CV of Pt$_{80}$Co$_{20}$ NW in H$_2$SO$_4$ (see Fig. 7C) does effectively show a $h_2/h_1$ peak current ratio larger than 1, but a more systematic study of the effect of the deposition potential on the H sorption properties of PtCo will be needed to clarify this issue. Therefore, it is not clear at this moment if the larger specific area of PtCo NWs prepared at −0.35 V is an intrinsic property of the deposit or an experimental artifact.



**Fig. 7.** Cyclic voltammograms of bimetallic CoPt TF ($\triangledown$) and NW ($\triangle$) in 0.5 M H$_2$SO$_4$ at 25 mV s$^{-1}$. The composition of the bimetallic deposit is (A) Co$_0$Pt$_{100}$, (B) Co$_{10}$Pt$_{90}$, (C) Co$_{20}$Pt$_{80}$ and (D) Co$_{40}$Pt$_{60}$.

Nevertheless, a close inspection of the data of Table 1 shows that the specific areas of NW at any given composition is a factor of five higher than the specific surface area of a thin film prepared at the same potential (same composition). This is clearly related to the 1D nanostructures (nanowires) that are formed when deposition is performed through an AAO membrane. The factor of ~5 increase of the specific current is lower than the factor (~20) expected based on a calculation involving only geometrical consideration (4 μm long NWs with ~300 nm diameter, arranged in a hexagonal lattice with a center-to-center distance of ~350 nm). However, it should be kept in mind that this calculation was made considering TFs with a roughness factor of ca 1. This is obviously not the case for bimetallic PtCo TFs (see Fig. 1) which explain the discrepancy between the actual and the expected increase of the specific current. Moreover, there is evidence in the literature that the entire length of the nanowires is accessible to the electrolyte. This was demonstrated by a significant decrease of the diameter of PbO$_2$ nanowire in contact with methanesulfonic acid when the electrode potential is changed from the charged to the discharged state [45]. In that medium, the discharge of PbO$_2$ occurs through the dissolution of Pb$^{+2}$ cations in methanesulfonic acid. This change of the diameter occurs on the entire length of each nanowire, indicating that the reduction reaction is not limited to the utmost outer portion of the nanowires. This is strong evidence that the electrolyte has access to the entire length of the nanowires. The same observation was made for PbO$_2$ nanowires in contact with sulfuric acid [46], and it is presumed that the same holds true in the case of bimetallic PtCo NWs in contact with H$_2$SO$_4$.

The electrocatalytic performance of the bimetallic PtCo TFs and NWs toward methanol oxidation was evaluated by cyclic voltammetry in a 0.5 M H$_2$SO$_4$ aqueous solution containing 1 M CH$_3$OH at room temperature. The CVs of Pt$_{90}$Co$_{10}$, which turns out to be the most interesting composition, are given as a representative example in Fig. 8. As seen in that figure, hydrogen adsorption and desorption is totally suppressed in the presence of methanol, indicating that methanol adsorption occurs at the surface of both deposits. As far as we can tell, all deposits behave similarly, independently of their composition and structure (TF or NW).

The onset for the electro-oxidation of methanol, $E_{onset}$, was estimated from the CV by recording the potential at which the current is a factor of 3 higher than the base line. There is not systematic variation of the $E_{onset}$ value with the composition of the bimetallic PtCo. However, the mean $E_{onset}$ value of CoPt TFs is 0.42 ± 0.06 V, while it is 0.33 ± 0.03 V for CoPt NWs. The oxidation of methanol on NW seems to begin at lower potential (less anodic) than on TF of the same composition. Although the $E_{onset}$ values of CoPt NWs are systematically lower than the corresponding value for PtCo TFs with the same composition, this assertion will need further confirmation since the difference between the mean onset values is equal to the sum of the uncertainties of the two values.

At potentials more positive than the onset potential, the current rises to reach a maximum at ca 0.70 V. This current is associated with the electro-oxidation of methanol. At higher potentials, the current drops because of the formation of platinum hydroxide that prevents the adsorption of methanol on the surface of the catalyst.
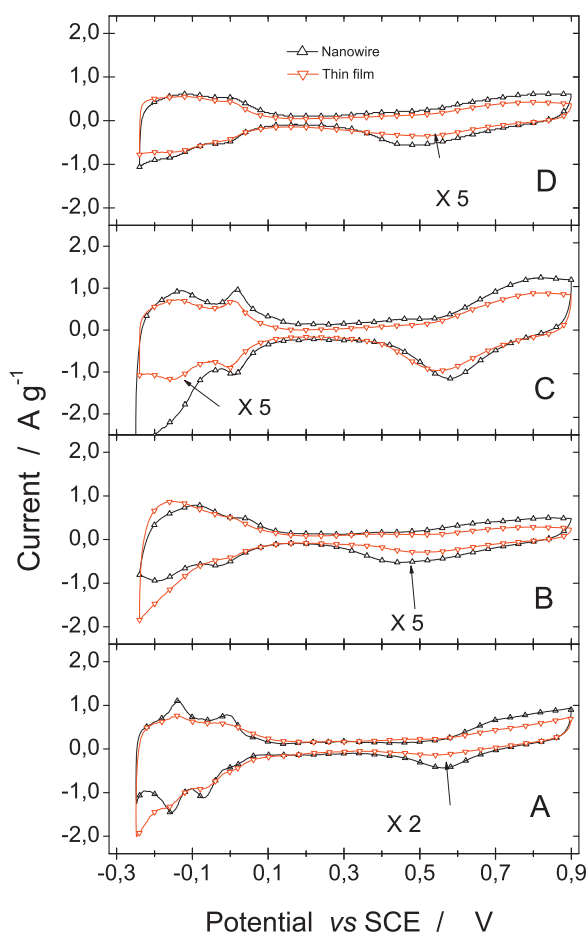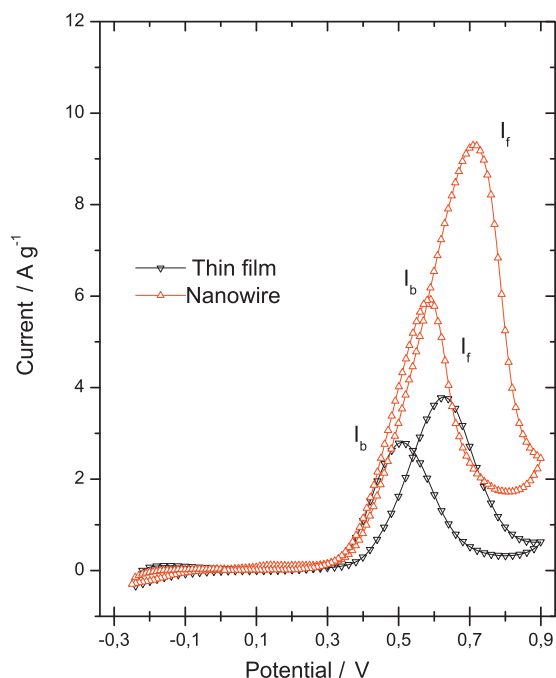
**Fig. 8.** Cyclic voltammograms of $Pt_{90}Co_{10}$ TF ($\triangledown$) and NW ($\triangle$) in 1.0 M $CH_3OH$ + 0.5 M $H_2SO_4$ at 5 mV s$^{-1}$.

On the reverse sweep, there is another oxidation peak that occurs concomitant with the removal of the hydroxyl groups from the surface. Similar curves (not shown) were obtained for the bimetallic PtCo TFs and NWs investigated in the present study.

The analysis of the CV for methanol oxidation on bimetallic CoPt was performed according to the method proposed by Mancharan and Goodenough [47]. In this analysis, the maximum current of the forward oxidation peak, $I_f$ at ca 0.7 V is attributed to the oxidation of methanol, whilst the maximum current of oxidation peak on the reverse sweep, $I_b$ at ca 0.6 V, is attributed to the oxidation of the carboneaous species formed at the surface of the catalysts during the oxidation of methanol. According to this analysis, a lower $I_f/I_b$ ratio is indicative of a higher coverage of the catalyst surface by CO, hence a higher poisoning during the electro-oxidation of methanol.

The $I_f/I_b$ ratio of the various bimetallic CoPt TFs and NWs is given in Table 1. For thin films, the $I_f/I_b$ ratio decreases steadily from 1.36 to 0.91 as the nominal Co content is increased from 10 to 20%. It then increases again to 1.01 for higher Co content (40 at%). In the case of the NW, the $I_f/I_b$ ratio decreases steadily from 1.59 to 0.79 as the nominal Co content is increased from 10 to 40%. By comparison, the literature reports $I_f/I_b$ value of 0.76–0.87 for pure platinum [30,48]. Thus the $I_f/I_b$ values found in the present study for bimetallic PtCo TFs and NWs are in most cases larger than those of Pt, which indicates a better resistance to CO poisoning of the electrode surface than for pure Pt. In the case of the $Pt_{90}Co_{10}$ TFs and NWs, the $I_f/I_b$ values exceed that of commercially available PtCo/C (E-TEK) catalysts, which is 1.32 [30]. They also exceed the $I_f/I_b$ values found on Pt-decorated nanoporous gold leaf, where the highest ratio (1.23) is achieved by the least-plated sample [48]. However, they are lower than the maximum value found for optimized $Pt_{52}Ru_{48}$/C catalysts ($I_f/I_b$ = 2.30) [49]. These results indicate that only a small amount of Co (10 at%) is needed to yield to a significant improvement of the resistance to poisoning by CO during the electro-oxidation of methanol and that the addition of larger amount of Co does not bring any beneficial effect in terms of resistance to poisoning when compared with pure Pt.

It is noteworthy that the $I_f/I_b$ ratio of Pt-rich nanowires is systematically higher than that of thin films with the same

composition, indicating a better resistance to CO poisoning of NWs as compared to TFs. This effect could be related to the morphology of the NWs as opposed to TFs. As mentioned earlier, CO is easier to oxidize on larger Pt particles than on smaller ones [18,22–24]. The positive shift of the CO-stripping potential as the particle size is decreased is attributed to the stronger bonding of CO to the surface of smaller particles and the concomitant decrease in CO diffusion and slow kinetics of OH groups generation [50,51]. It was also suggested by Arenz et al. that the oxidation of CO in CO stripping experiment is mainly controlled by the number of defect sites on the structure [23]. According to them, the number of defects increases with the particle size and the ability of the surface to dissociate water and form $OH_{ads}$ on defect sites is increased. Therefore, CO oxidation is facilitated on larger particles.

The reasons of the better resistance to CO-poisoning of NW as compared to TF are not exactly known. As discussed previously, micrometer long NWs are formed when deposition is performed through an AAO membrane. The diffusion of CO and OH species at the surface of these elongated structures will be more favorable than on the less extended ones composing the thin films. Also, according to the previous discussion, it is expected that NW with a diameter of 280 nm will have several defect sites that could act to dissociate water molecules and form $OH_{ads}$. Both hypotheses can thus explain the observation made earlier than NW exhibit a better resistance to CO poisoning than TF of the same composition.

## 4. Conclusion

It was show that bimetallic PtCo thin films and nanowires can be prepared over the whole composition range from a common electroplating solution by changing the electrode potential. This work was mainly concerned with Pt-rich deposit ([Pt] $\geq$ 60 at%) that can be prepared in a potential region ($E_{dep} \geq -0.60$ V vs SCE) where bulk Co deposition does not occur. In that potential region, deposition of Co on Pt is non-nernstian and occurs as a result of underpotential deposition. The composition of thin films and nanowires prepared at the same potential is identical, indicating that the AAO membrane does not have significant influence on the diffusivity of $Pt^{4+}$ and $Co^{2+}$ cations. The deposition rates of Pt and of Co UPD on Pt were measured as a function of the electrode potential and it was shown that these deposition rates can be used to predict the actual composition of both thin films and nanowires prepared at any given potential. Upon deposition, an alloy is formed between Co and Pt, independently of the composition ([Pt] $\geq$ 60 at%) and structure (TF or NW) of the deposit. The results show that PtCo nanowires yield to an enhancement (by a factor of 5) of the exposed surface area (m$^2$ g$^{-1}$). In the presence of $CH_3OH$, the $I_f/I_b$ ratio of Pt-rich nanowires is systematically higher than that of thin films with the same composition, indicating a better resistance to CO poisoning of the electrode surface.

## References

[1] X. Ren, P. Zelenay, S. Thomas, J. Davey, S. Gottesfeld, J. Power Sources 86 (2000) 111–116.

[2] E. Reddington, A. Sapienza, B. Gurau, R. Viswanathan, S. Sarangapani, E.S. Smotkin, T.E. Mallouk, Science 280 (1998) 1735–1737.
[3] T. Iwasita, F.C. Nart, J. Electroanal. Chem. 317 (1991) 291–298.
[4] T.D. Jarvi, S. Sriramulu, E.M. Stuve, J. Phys. Chem. B 101 (1997) 3649–3652.
[5] A. Heinzel, V.M. Barragan, J. Power Sources 84 (1999) 70–74.
[6] J. Cruickshank, K. Scott, J. Power Sources 70 (1998) 40–47.
[7] K. Ramya, K.S. Dhathathreyan, J. Electroanal. Chem. 542 (2003) 109–115.
[8] N.M. Markovic, H.A. Gasteiger, P.N. Ross, X. Jiang, I. Villegas, M.J. Weaver, Electrochim. Acta 40 (1995) 91–98.
[9] S.L.J. Gojkovic, T.R. Vidakovic, D.R. Durovic, Electrochim. Acta 48 (2003) 3607–3614.
[10] T. Iwasita, Electrochim. Acta 47 (2002) 3663–3674.
[11] P.A. Christensen, A. Hamnett, G.L. Troughton, J. Electroanal. Chem. 362 (1993) 207–218.
[12] V.R. Stamenkovic, B.S. Mun, K.J.J. Mayrhofer, P.N. Ross, N.M. Markovic, J. Am. Chem. Soc. 128 (2006) 8813–8819.
[13] L.J. Bregoli, Electrochim. Acta 23 (1978) 489–492.
[14] K. Kinoshita, J. Electrochem. Soc. 137 (1990) 845–848.
[15] N. Giordano, E. Passalacqua, L. Pino, A.S. Arico, V. Antonucci, M. Vivaldi, K. Kinoshita, Electrochim. Acta 36 (1991) 1979–1984.
[16] Y. Takasu, N. Ohashi, X.G. Zhang, Y. Murakami, H. Minagawa, S. Sato, K. Yahikozawa, Electrochim. Acta 41 (1996) 2595–2600.
[17] H.A. Gasteiger, S.S. Kocha, B. Sompalli, F.T. Wagner, Appl. Catal. B: Environ. 56 (2005) 9–35.
[18] K.J.J. Mayrhofer, B.B. Blizanac, M. Arenz, V.R. Stamenkovic, P.N. Ross, N.M. Markovic, J. Phys. Chem. B 109 (2005) 14433–14440.
[19] K.J.J. Mayrhofer, D. Strmcnik, B.B. Blizanac, V. Stamenkovic, M. Arenz, N.M. Markovic, Electrochim. Acta 53 (2008) 3181–3188.
[20] Z. Chen, M. Waje, W. Li, Y. Yan, Angew. Chem. Int. Ed. 46 (2007) 4060–4063.
[21] H. Zhou, W.P. Zhou, R.R. Adzic, S.S. Wong, J. Phys. Chem. C 113 (2009) 5460–5466.
[22] F. Maillard, E.R. Savinova, P.A. Simonov, Z.I. Zaikovskii, U. Stimming, J. Phys. Chem. B 108 (2004) 17893–17904.
[23] M. Arenz, K.J.J. Mayrhofer, V. Stamenkovic, B.B. Blizanac, T. Tomoyuki, P.N. Ross, N.M. Markovic, J. Am. Chem. Soc. 127 (2005) 6819–6829.
[24] Z. Liu, M. Shamsuzzoha, E.T. Ada, W.M. Reichert, D.E. Nikles, J. Power Sources 164 (2007) 472–480.
[25] A. Ponrouch, S. Garbarino, D. Guay, Electrochem. Commun. 11 (2009) 834–837.
[26] S. Garbarino, A. Ponrouch, D. Guay, Electrochem. Commun. 11 (2009) 1449–1452.
[27] A. Ponrouch, M.P. Bichat, S. Garbarino, C. Maunders, G. Botton, P.-L. Taberna, P. Simon, D. Guay, ECS Trans. 25 (2010) 3–11.
[28] A. Ponrouch, S. Garbarino, S. Pronovost, P.L. Taberna, P. Simon, D. Guay, J. Electrochem. Soc. 157 (2010) K59–K65.
[29] J.J. Mallett, E.B. Svedberg, S. Sayan, A.J. Shapiro, L. Wielunski, T.E. Madey, P.J. Chen, W.F. Egelhoff Jr., T.P. Moffat, Electrochem. Solid State Lett. 8 (2005) C15–C18.
[30] L. Liu, E. Pippel, R. Scholz, U. Gösele, Nanoletters 9 (2009) 4352–4358.
[31] K. Jayasayee, V.A.T. Dam, T. Verhoeven, S. Celebi, F.A. De Bruijn, J. Phys. Chem. C 113 (2009) 20371–20380.
[32] P.J. Ferreira, G.J. La O', Y. Shao-Horn, D. Morgan, R. Makharia, S. Kocha, H.A. Gasteiger, J. Electrochem. Soc. 152 (2005) A2256–A2271.
[33] L.H. Mendoza-Huizar, J. Robles, M. Palomar-Pardavé, J. Electroanal. Chem. 512 (2002) 95–106.
[34] L.H. Mendoza-Huizar, J. Robles, M. Palomar-Pardavé, J. Electroanal. Chem. 545 (2003) 39–45.
[35] L.H. Mendoza-Huizar, J. Robles, M. Palomar-Pardavé, J. Electrochem. Soc. 152 (2005) C265–C271.
[36] A. Montes-Rojas, L.M. Torres-Rodriguez, C. Nieto-Delgado, New J. Chem. 31 (2007) 1769.
[37] L.H. Mendoza-Huizar, C.H. Rios Reyes, J. Solid State Electrochem. 15 (2011) 737–745.
[38] S. Koh, J. Leisch, M.F. Toney, P. Strasser, J. Phys. Chem. C 111 (2007) 3744–3752.
[39] E. Antolini, J.R.C. Salgado, E.R. Gonzalez, Appl. Catal. B: Environ. 63 (2006) 137–149.
[40] Y. Saejeng, N. Tantavichet, J. Appl. Electrochem. 39 (2009) 123–134.
[41] F. Wang, K. Hosoiri, S. Doi, N. Okamoto, T. Kuzushima, T. Totsuka, T. Watanabe, Electrochem. Commun. 6 (2004) 1149–1152.
[42] R. Juskenas, Z. Mockus, S. Kanapeckaite, G. Stalnionis, A. Survila, Electrochim. Acta 52 (2006) 928–935.
[43] B.D. Cullity, Elements of X-ray Diffraction, 2nd edition, Addison-Wesley, 1978.
[44] S. Garbarino, A. Ponrouch, S. Pronovost, J. Gaudet, D. Guay, Electrochem. Commun. 11 (2009) 1924–1927.
[45] P. Perret, Z. Khani, T. Brousse, D. Bélanger, D. Guay, Electrochim. Acta 56 (2011) 8122–8128.
[46] P. Perret, T. Brousse, D. Bélanger, D. Guay, J. Electrochem. Soc. 156 (2009) A645–A651.
[47] R. Mancharan, J.B. Goodenough, J. Mater. Chem. 2 (1992) 875–887.
[48] X. Ge, R. Wang, P. Liu, Y. Ding, Chem. Mater. 19 (2007) 5827–5829.
[49] Z. Liu, X.Y. Ling, X. Su, J.Y. Lee, J. Phys. Chem. B 108 (2004) 8234–8240.
[50] K.A. Friedrich, F. Henglein, U. Stimming, W. Unkauf, Electrochim. Acta 45 (2000) 3283–3293.
[51] K.A. Friedrich, F. Henglein, U. Stimming, W. Unkauf, Electrochim. Acta 47 (2001) 689–694.